Corrosion Science 100 (2015) 365–376

Contents lists available at ScienceDirect

Corrosion Science

journal homepage: www.elsevier.com/locate/corsci

The corrosion inhibition effect of phytic acid on 20SiMn steel in simulated carbonated concrete pore solution

Fengting Cao, Jie Wei, Junhua Dong*, Wei Ke

State Key Laboratory for Corrosion and Protection, Institute of Metal Research, Chinese Academy of Sciences, Shenyang, China

ARTICLE INFO

Article history:
Received 18 May 2015
Received in revised form 3 August 2015
Accepted 5 August 2015
Available online 8 August 2015

Keywords:
A. Steel reinforced concrete
B. SEM
B. XPS
B. EIS
C. Neutral inhibitor

ABSTRACT

The corrosion inhibition effect of phytic acid on 20SiMn steel in simulated carbonated concrete pore solution contaminated by Cl^- was investigated by weight loss, electrochemical measurements, scanning electron microscope (SEM), X-ray photoelectron spectroscopy (XPS) and Raman spectroscopy. Results show that the inhibition efficiency of IP6 is up to 84.0% after 72 h immersion. An deposited film forms on the surface of specimen after the addition of IP6, which includes three layers: the inner layer consists of Fe_3O_4 and FeOOH; the middle layer contains Fe_3O_4, FeOOH and $FePO_4$; the outer layer consists of Fe_3O_4, FeOOH, $FePO_4$ and Fe(II)-IP6.

1. Introduction

With high strength, great flexibility and low-cost, reinforced concrete structures have been widely used in many fields since 19th century. Under normal conditions, the steel rebar is free from corrosion because of the passive film formed in the concrete pore solution of high alkalinity [1]. However, if chlorides diffuse through the concrete to the steel surface and accumulate to a certain concentration [2] and/or the carbonation occurs caused by CO_2, the corrosion of rebar will be induced [3], leading to premature deterioration and final failure of the reinforced concrete structures. It is well-known that carbonation of concrete is the result of the dissolution of CO_2 in the concrete pore solution and this reacts with calcium from calcium hydroxide and calcium silicate hydrate to form calcite ($CaCO_3$). Carbonation is associated with the corrosion of steel rebar and with shrinkage. However, it also increases both the compressive and tensile strength of concrete, so not all of its effects on concrete are bad. Due to the low solubility of $CaCO_3$ (K_{sp} of calcite = 3.4×10^{-9}), virtually all (>99.9%) of the calcium ions precipitate out. With the carbonation process go on, part of $CaCO_3$ further react with CO_2 to produce the soluble $Ca(HCO_3)_2$ and to decrease the pH value of the pore solution. Under this circumstance, the free anion of HCO_3^- will make an important effect on the corrosion of the steel rebar, and the released free Ca^{2+} normally does not participate in the electrochemical reactions. Accordingly, ($NaHCO_3 + Na_2CO_3$) buffer solution is usually to be used as the simulated carbonated concrete pore solution [4–6].

Several techniques have been employed to reduce the corrosion of steel rebar so far, such as coatings, cathodic protection, waterproofing membrane, inhibitors, etc. Among all the techniques available, inhibitors are remarkable for their advantages, such as high efficiency and easy handling. In general, inhibitors used for steel rebar in concrete include nitrites [7–9], sodium mono-fluorophosphate (MFP) [10], amines and alkanolamines (AMAs) [11,12] etc. and other inorganic [13] or organic compounds [14] or mixtures. Nevertheless, these inhibitors have been considered to be toxic and poor inhibiting effect in the case of insufficient dosage for nitrites, diffusion difficulty for MFP [15], and the disagreement of the inhibiting mechanism of some AMAs [16,17], which restrict their applications. Hence, developing new kinds of environmental-friendly inhibitors with high efficiency for concrete rebar becomes a necessary research subject.

So far, most of the studies [18,4] on steel inhibitor in high pH concrete pore solution were just focused on the initial corrosion stage when the steel is passivated. Nevertheless, the pH will gradually decrease to near neutral scope induced by the carbonation, which will cause the dissolution of passive film and the exposure of steel substrate. Accordingly, it's necessary to study inhibitors against the corrosion in this stage but few works were carried out in the past [4]. Compared to the traditional inhibitors, phytic acid (IP6) and its salts seem to be more attractive for steel rebar because this kind of substance is non-poisonous and low-cost. Phytic acid, a

* Corresponding author. Fax: +86 24 23894149.
E-mail address: jhdong@imr.ac.cn (J. Dong).

http://dx.doi.org/10.1016/j.corsci.2015.08.020
0010-938X/

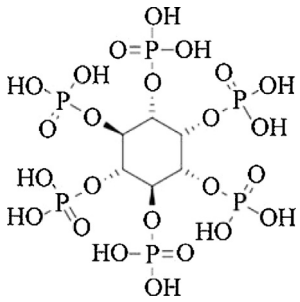

Fig. 1. Structure of phytic acid.

saturated cyclic acid, consists of 6 phosphate carboxyl groups (see Fig. 1) [19], resulting in a powerful chelating ability with many metal ions, such as Cu^{2+}, Zn^{2+} Mg^{2+}, Ca^{2+}, Fe^{2+} and Fe^{3+} [20]. Up to date, IP6 and its salts have been used as additive agent for copper and its alloys [21–25], magnesium alloys [26–28], aluminium alloys [29], etc., and their anticorrosive efficiency could reach 90% or more. In addition, the inhibiting mechanisms of IP6 for the metals mentioned above have been studied and can be classified into two types in general: one is to form an adsorption film of IP6 on metal surface by chemisorption [30–32] and the other is to act as a conversion coating by forming complexes with metal ions [26,27,33]. However, few works could be found in literature concerning the inhibiting effect and mechanism of IP6 on carbon steel in simulated concrete solutions. Considering the capability to chelate with Fe^{2+} and Fe^{3+} [20], it should be meaningful to investigate the inhibition effect of IP6 in a near neutral concrete simulated solution on steel rebar.

In the present work, the effectiveness of IP6 as corrosion inhibitor on 20SiMn steel has been tested in buffer bicarbonate solutions contaminated with chlorides through weight loss and electrochemical tests. Particularly, the evolution of the inhibiting film was investigated, and finally a suitable mechanism of corrosion inhibition was proposed.

2. Experimental

2.1. Materials and solutions

Material used for this work was 20SiMn steel (wt.%: C 0.21, Si 0.5, Mn 1.43, P 0.022, S 0.028 and balance Fe), a kind of low-alloy steel with higher corrosion resistance than carbon steel widely used in the reinforced concrete structures. The size of the specimens was 5.0 cm × 1.0 cm × 0.25 cm. The inhibitor IP6 was purchased in the form of aqueous solution with 70 wt.% concentration as high grade reagent. Fig. 1 shows the molecular structure of IP6. All other chemicals were of analytical grade from China-Reagent Group. The electrolyte solutions were simulated carbonated pore concrete solutions without and with inhibitor: S0 (0.045 mol/L $NaHCO_3$ + 0.005 mol/L Na2CO3 + 0.6 mol/L NaCl) and S1 (0.045 mol/L $NaHCO_3$ + 0.005 mol/L Na_2CO_3 + 0.6 mol/L NaCl + 5.30 mmol/L IP6), and the pH values of S0 and S1were 8.9. All the measurements were carried out in open-air conditions at room temperature around 30 ± 1 °C.

2.2. Weight loss measurements

Specimens were mechanically ground with silicon carbide papers from 80 to 1000 grit, cleaned with deionized water and absolute ethyl alcohol, then dried with cold air. Previously weighed specimens were suspended and immersed totally into S0 and S1. Each container held three parallel specimens and the solutions were kept in aerated conditions. The specimens were withdrawn after 72 h immersion. The corrosion products were removed by running water, a 20% HCl plus 5% methenamine solution and acetone successively. Afterwards, the specimens were washed with deionized water and finally dried and reweighed. The corrosion rate (ν) and inhibition efficiency (η%) were calculated through the following equations [34]:

$$\nu(\mathrm{gm^{-2}h^{-1}}) = \frac{\Delta W}{St} \tag{1}$$

$$\eta(\%) = \frac{\nu_0 - \nu_1}{\nu_0} \times 100 \tag{2}$$

where η is the inhibition efficiency, ΔW the weight loss of sample (g), S the total surface area of the sample (m^2), t the immersion time (h), ν_0 and ν_1 the corrosion rates of sample in the absence and presence of inhibitor, respectively. The corrosion rate (ν) can also be expressed in the unit of mm/a:

$$\nu\left(\frac{\mathrm{mm}}{a}\right) = \frac{8.76\Delta W}{StD} \tag{3}$$

where D is the density of material (for 20SiMn steel is 7.85 g/cm^3).

2.3. Electrochemical measurements

A Gamry DC105 electrochemical workstation and a classical three-electrode cell were used for the electrochemical measurements. The 20SiMn steel was used as working electrode (WE), with a copper wire welded to its back and embedded in epoxy resin. The exposed working area was 1.0 cm × 1.0 cm. The specimens were also ground and cleaned under the same conditions with weight loss measurements. A platinum plate and the saturated calomel electrode (SCE) were used as the counter electrode (CE) and the reference electrode (RE), respectively. Potentiodynamic polarization curves were measured at a scan rate of 0.166 mV/s. Before each test, the working electrode was kept in solutions at open circuit potential for 0.5, 6, 24, 36 and 72 h, separately. The inhibitive efficiency (η%) was calculated through the following equation [34]:

$$\eta(\%) = \frac{I_{corr,0} - I_{corr,1}}{I_{corr,0}} \times 100 \tag{4}$$

where $I_{corr,0}$ and $I_{corr,1}$ are the corrosion current density at the absence and presence of IP6, respectively.

The electrochemical impedance spectroscopy (EIS) was in *situ* measured in the parallel immersion test corresponding to the time of each potentiodynamic polarization curve measurement. The frequency was ranged from 10 kHz to 10 mHz with an amplitude of 10 mV AC signals at open circuit potential (OCP) in a steady state, and the EIS data was fitted using the ZSimpWin software. There were 7 steps/decade in the EIS measurements. Generally, the corrosion current density of the rebar can be approximately calculated according to Stern–Geary equation:

$$I_{corr} = \frac{B}{R_{ct}} \tag{5}$$

where I_{corr} (μA/cm^2) represents the corrosion current density and B the "Stern–Geary constant". The value of B is often used as 52 mV and 26 mV in the calculation for rebar in the passive and active states, respectively. In this paper, since the corrosion of 20SiMn steel is in an active state, the value of B is assigned as 26 mV. Additionally, the corrosion rate ν(mm/a) can also be calculated by substituting I_{corr} taken from potentiodynamic polarization curves and EIS:

$$\nu\left(\frac{\mathrm{mm}}{a}\right) = \frac{0.00327aI_{corr}}{nD} \tag{6}$$

where a is the molar mass of steel (here is approximately assign as iron of 56 g/mol), and n the charge transfer number of the reactant (here is 2).

The inhibition efficiency (η%) was calculated through the following equations [34]:

$$\eta(\%) = \frac{R_{ct,1} - R_{ct,0}}{R_{ct,1}} \times 100 \quad (7)$$

where $R_{ct,0}$ and $R_{ct,1}$ are charge transfer resistances at the absence and presence of IP6, respectively.

The OCP of specimens during this immersion test was monitored by a HA–151A potentiostat. All potential values were versus SCE unless specially noted. Each electrochemical test was conducted at least twice for repeatability.

2.4. Surface analysis

Inspect TMF scanning electron microscopy (SEM) equipped with energy dispersive X-ray analysis was employed to observe the morphologies (SE) of specimens in S0 and S1 for 72 h and the films of specimens in S1 for 6, 36 and 72 h (BSE). X-ray photoelectron spectroscopy (XPS Thermo Elctron-former VG ESCALAB 250) was used to analyze the corrosion product of the specimen immersed in S1 solution for 72 h, and a monochromated Al KαX-ray source (1486.6 eV, pass energy of 50 eV, power of 150 W) was employed. The specimen was etched by ionized argon in the chamber at a vacuum of 6×10^{-8} mbar and the etching rate was 0.2 nm/s. All binding energy data in the XPS spectra were corrected by fixing the C1s peak at the standard binding energy (284.6 eV). The data were fitted using the XPSPEAK Version 4.1 software.

Raman spectra from 50 cm^{-1} to 2000 cm^{-1} were used to analyze composition of the corrosion products of the specimen immersed in S0 and S1 for 2, 24 and 72 h separately. The measurement was conducted using a conventional scattering technique under the 632.8 nm line of a Melles Griot 35 mW HeNe laser, which was focused on the specimen through an Olympus microscope with a 50× magnification objective lens. Raman spectra data were collected on at least three representative spots for one specimen to make sure the reproducibility of the spectra.

3. Results and discussion

3.1. Immersion test and morphologies

Table 1 lists the weight loss results of three parallel specimens after immersed in S0 and S1 for 72 h. It can be seen that the corrosion rate evidently decreases after introducing the inhibitor IP6. The average corrosion rate of the specimen immersed in S0 and S1 is 0.162 and 0.026 mm/a, respectively, and the corresponding inhibition efficiency (η) calculated by Eq. (2) reaches to 84.0%. It is widely acknowledged that as the corrosion rate of rebar in concrete is lower than 0.002 mm/a, the corrosion can be negligible. Obviously, the corrosion of 20SiMn steel in the simulated carbonated concrete pore solution is not completely suppressed by IP6, but it has been significantly alleviated.

Fig. 2(a–c) show the optical photos of 20SiMn steel before (a) and after immersed in the solutions with respect to S0 (b) and S1 (c) for 72 h. As can be seen, a thick corrosion product layer with black and brown color grows on the specimen surface in S0, while a thin milk-white layer forms in S1. Fig. 2(a′–c′) show the micro-morphologies of 20SiMn steel corresponding to the optical photos, respectively. Obviously, the corrosion product layer grown on the specimen surface in S0 appeares a loose morphology and two shapes of particles, one is hexagon and another one is flocculent, which may be corresponding to different chemical substance. Different from the specimen immersed in S0, that immersed in S1 shows a uniform and compact layer formed on the surface.

Fig. 3 shows the BSE images of the cross-section of specimens in S1 for 6, 36 and 72 h, respectively. It indicates that the film thickens with the increasing immersion time. After immersed for 6 h, the cross-section morphology of the film is loose and discontinuous, which indicates that the deposited film has not completely covered over the specimen surface. After immersed for 36 h, the cross-section morphology shows that the completeness of this deposited film has achieved, with the thickness of around 500–700 nm. When the steel was immersed for 72 h, the deposited film became more compact and uniform with the thickness of around 800–1000 nm.

3.2. Raman spectroscopy

During the immersion test in S0 and S1 solutions, Raman spectroscopy were measured at different time, shown in Fig. 4, and the band component database are listed in Table 2. According to Fig. 4, the hexagon component shown in Fig. 2(b′)reveals three Raman shift peaks at 208, 418 and 503 cm^{-1}, successively. These bands are assignable to FeOOH [35]. As for the flocculent component also shown in Fig. 2 (b′), the only observed band at 715 cm^{-1} can be ascribed to Fe_2O_3 [35]. With respect to the specimen immersed in S1 solution for different time, all of Raman spectra show similar Raman shift peaks, implying that the corrosion products formed at different time have similar chemical compositions. The peaks located at 288 cm^{-1} for 2 h, 286 cm^{-1} for 24 h and 297 cm^{-1} for 72 h are ascribed to Fe_3O_4 [35], while 386 cm^{-1} for 2 h, 392 cm^{-1} for 24 h and 418 cm^{-1} for 72 h are assigned to FeOOH [35]. These peaks suggest that iron oxides have already existed in the deposited film at the initial of the immersion test. With regards to the bands observed at 430 and 557 cm^{-1} in the Raman spectra, it could be assigned to the in-plane and out-plane vibrations of PO_4 unit [36], respectively. As for the comparatively broad peak exhibited in the region of 900–1200 cm^{-1}, it could be divided into three peaks at 1005, 1078 and 1161 cm^{-1}. The peak located at 1005 cm^{-1} belongs to the symmetric stretching vibrations of the PO_4 units, while those at 1078 and 1161 cm^{-1} are assigned to the antisymmetric stretching vibrations of PO_4 units [36]. The emergence of these characteristic bands proves the presence of phosphate in the corrosion products. In addition, the peak appeared at 578 cm^{-1} could be assigned to the stretching vibration of C—O—P [37], and that at 1318 cm^{-1} should be assigned to the stretching vibration of P—O [31]. The band located at around 1445 cm^{-1} may be originated from the combination stretching vibration of C═O and bending vibrations of C—CC and C—H [30], while that at 1576 cm^{-1} could be assigned to the asymmetrical deformation vibration of six-member ring generated from IP6 [37]. These peaks of C—O—P, P—O, C—C—C, C—H, especially six-member ring directly demonstrate the participation of IP6 in the deposited film. IP6 could chelate with Fe^{2+} and other metal ions, and this has been reported by other researchers [20]. Therefore, the presence of complex Fe(II)-IP6 could be inferred.

3.3. X-ray photoelectron spectroscopy analyses

Fig. 5 shows the survey spectra and the elemental depth profile of X-ray photoelectron spectroscopy (XPS) analyses for the deposited film. Obviously, the deposited film is composed of Fe, C, P and O elements. The survey spectra indicate that the peak intensities of C1s, P2p and O1s gradually decrease with the increase of etching time. To be specific, the survey spectrum of C1s disappears after about 100 s, those of P2p disappear after 3500 s, corresponding to the etching depth of 200 and 700 nm, respectively, while those of O1s still emerge even after etching about 5900 s. In addition, the band energy of Fe2p presents two overlapped peaks in the outside film, and it gradually changes to a single peak in the most inner layer of the film. This implies that Fe has formed several compounds with different valences in the film. Furthermore, the peak intensity of Fe2p gradually increases with the increase of etching time, for the etching is toward to the steel substrate.

Table 1
Weight loss results in the absence (v_0) and presence (v_1) of 5.30 mmol/L IP6 for 72 h immersion, recorded in (0.045 mol/L $NaHCO_3$ + 0.005 mol/L Na_2CO_3 + 0.6 mol/L NaCl) solution.

Parallel specimens	v_0/g m^{-2} h^{-1}	v_0/mm a^{-1}	v_1/g m^{-2} h^{-1}	v_1/mm a^{-1}	η/%
1	0.150	0.166	0.028	0.031	
2	0.141	0.157	0.026	0.029	
3	0.145	0.162	0.016	0.018	
Average	0.145	0.162	0.023	0.026	84.0

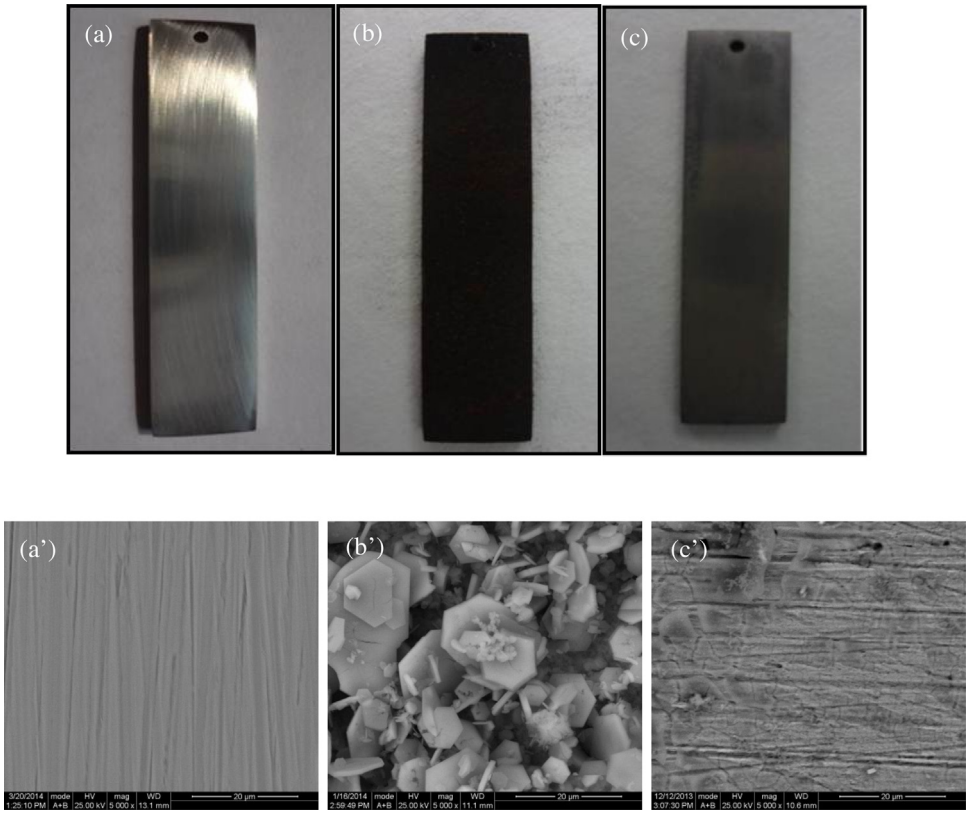

Fig. 2. Optical photos and micro-morphologies of 20SiMn steel rebar before (a, a') and after immersed in the absence (b, b') and presence (c, c') of 5.30 mmol/L IP6 for 72 h, recorded in (0.045 mol/L $NaHCO_3$ + 0.005 mol/L Na_2CO_3 + 0.6 mol/L NaCl) solution.

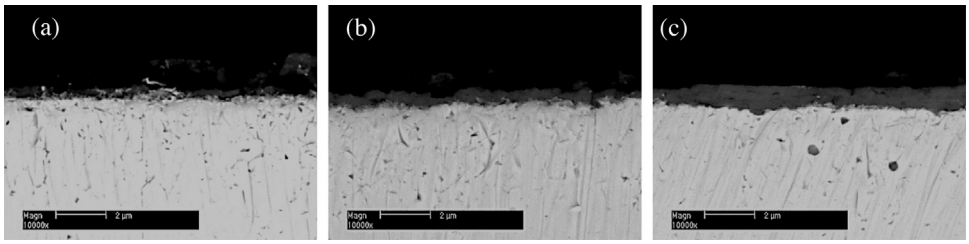

Fig. 3. BSE (SEM) images of cross-section of the specimen immersed in the presence of 5.30 mmol/L IP6 for 6 h (a), 36 h (b) and 72 h (c), recorded in (0.045 mol/L $NaHCO_3$ + 0.005 mol/L Na_2CO_3 + 0.6 mol/L NaCl) solution.

Besides, the elemental depth profile in Fig. 5b indicates that the elemental atomic ratio of C, P and O in the film does not accord with that of in phytic acid molecule, C:P:O = 1:1:6, and the content of P is far higher than that of C. Since IP6 is the only source of P element in the deposited film in S1, it could be inferred that IP6 has been hydrolyzed. Additionally, the disappearance of P prior to oxygen after etching for about 3500 s (Fig. 5a) suggests that the most inner layer is mainly composed of iron oxides. Consequently, the deposited film could be simply divided into three layers according to the elements distributions: the outer layer with C, P, Fe, O; the middle layer with P, Fe, O; and the inner layer only with Fe, O.

Fig. 6(a–d) shows the XPS high-resolution spectra of Fe2p, O1s, P2p, C1s of the film deposited in S1 after etching for 10, 740, 2000 and 3500 s, successively. The patterns at different etching time are suggested to represent the distribution of the chemical species along the film thickness. The XPS spectra of Fe2p etching for 10 s could be fitted with five peaks at 706.3, 707.4, 709.1, 710.7 and 712.9 eV. The smaller peak located peak at 706.3 eV is belonged to metallic iron [38] that maybe generated from the reduction of iron oxides by ionized argon in XPS measured process. Based on the analysis of Raman spectra above, it is clearly that IP6 has participated into the formation of the deposited film. Furthermore, it is

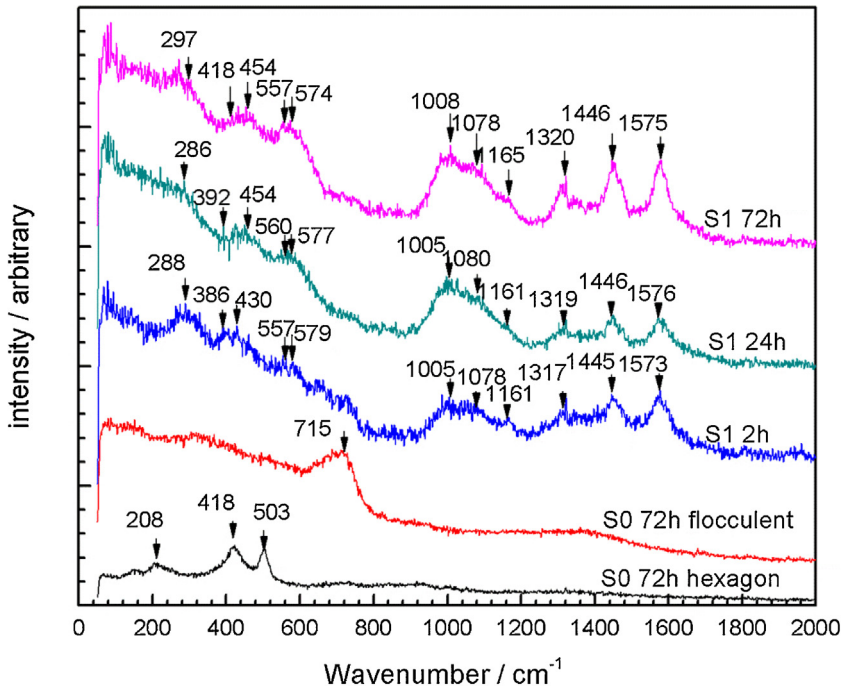

Fig. 4. Raman spectra of the specimens in the absence (S0) of IP6 for 72 h and those in the presence (S1) of 5.30 mmol/L IP6 for 2 h, 24 h and 72 h, recorded in (0.045 mol/L $NaHCO_3$ + 0.005 mol/L Na_2CO_3 + 0.6 mol/L NaCl) solution.

reported [27,29,39] that IP6 is likely to chelate with divalent cations to form complex. Hence, it could be referred that the peak located at 707.4 eV is assigned to Fe(II)-IP6. Generally, Fe2p band energies of ferrous and ferric oxides are mainly in the range of around 708–709.5 eV and 710.5–711 eV, respectively, and ferric hydroxide around 711.5–712 eV [40]. Accordingly, the peak at 709.1 is assigned to Fe_3O_4 [41] and that at 710.7 is corresponding to FeOOH [42]. Moreover, the peak with the highest binding energy 712.9 eV is ascribed to iron phosphate $FePO_4$ [43]. At the same time, the XPS of O1s etching for 10s provides additional useful information for determination of the composition of the outer layer. As can be seen, the broad complex XPS peak of O1s spectrum is fitted by the weighted stacking of four sub-peaks. According to the literature [39], the peak of O1s with binding energy values of (530.2 ± 0.3) and (532.1 ± 0.3) eV could be assigned to P–O–C and P–O–Metal (II), respectively. Therefore, the peak located at 530.1 eV should be assigned to the complex Fe(II)-IP6, while that located at 531.8 eV belonged to $FePO_4$ [44]. The other two peaks at 530.7 and 531.3 eV could be ascribed to Fe_3O_4 [41] and FeOOH [45], respectively. Moreover, the XPS spectra of P2p can be decomposed into two peaks located at 132.9 eV [46] and 133.7 eV [44], corresponding to P3/2 and P1/2 in phosphate group (PO_4), respectively. This response can be generated from either $FePO_4$ or Fe(II)-IP6, for P is in a similar chemical environment in both compounds [39]. The XPS spectra of C1s with binding energy values of 284.6 eV and 284.1 eV could be assigned to free carbon and CC [47] in IP6, respectively. It proves the presence of IP6 in the deposited film. Based on the above analysis, it could be conclude that the outer layer is consisted of Fe(II)-IP6, $FePO_4$, FeOOH and Fe_3O_4. However, with increasing the etching time, the XPS spectra of Fe2p and O1s show that the high-solution peaks of Fe(II)-IP6, $FePO_4$ and FeOOH are respectively disappeared at 740, 2000 and 3500s. Obviously, the middle layer in the deposited film is composed of $FePO_4$, FeOOH and Fe_3O_4, the inner layer consists of FeOOH and Fe_3O_4, and the most inner layer close to steel substrate is mainly Fe_3O_4. It's reasonable for this distribution of the chemical species and it agrees with the Raman spectra results. The insoluble products could suppress the diffusion of aggressive ions including Cl^-, O_2, and finally reduce the iron dissolution. The chemical conversion films with similar chemical components such as $FePO_4$, FeOOH and Fe_3O_4 have also been obtained in inorganic

Table 2
Assignments database for the total observed Raman bands of specimens immersed in the absence (S0) and presence (S1) of 5.30 mmol/L IP6 for different immersion time, recorded in (0.045 mol/L $NaHCO_3$ + 0.005 mol/L Na_2CO_3 + 0.6 mol/L NaCl) solution.

Iron oxides		Ligand	
Raman shift	Assignment	Raman shift	Assignment
715	Fe_2O_3 [35]	1575	δAs(cyclring) [37]
503	FeOOH [35]	1446	ν(CO) + δ(CCC) + δ(CH) + δ(CH)[30]
418		1319	ν(P–O) [31]
386		1161	As(PO_4)[36]
392		1080	
208		1005	s(PO_4) [36]
297	Fe_3O_4[35]	577	ν(C–O–P) [37]
288		557	γ (PO_4) [36]
		454	β (PO_4) [36]
		430	

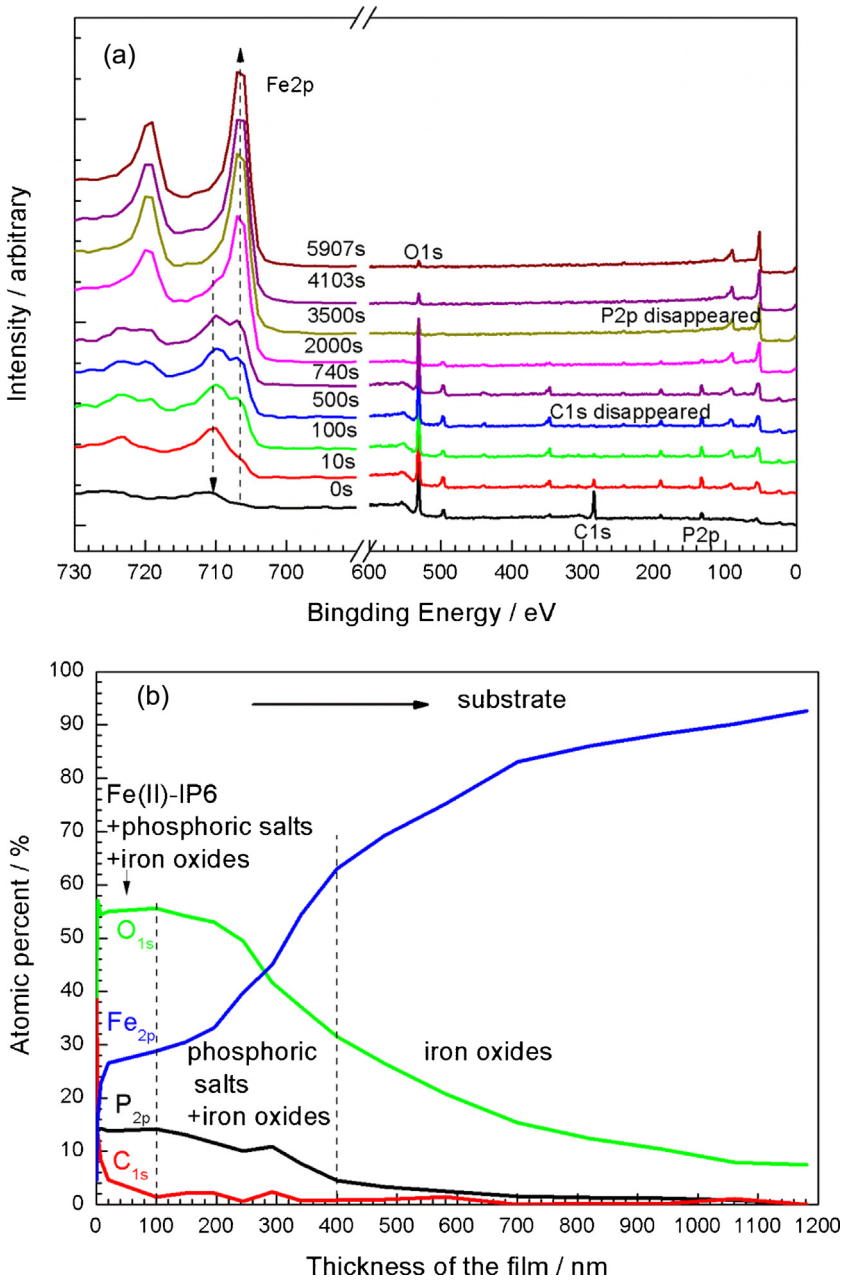

Fig. 5. XPS survey spectra with different sputtering times (a) and elemental depth profiles (b) of the film on the specimen immersed in the presence (S1) of 5.30 mmol/L IP6, recorded in (0.045 mol/L $NaHCO_3$ + 0.005 mol/L Na_2CO_3 + 0.6 mol/L NaCl) solution.

phosphate solutions [48–50]. Nevertheless, these films do not consist of the hydrolysis products of IP6, like Inositol phosphate, etc., which can lead to a difference in the corrosion inhibition from IP6.

3.4. Electrochemical measurements

3.4.1. Potentiodynamic polarization curves

Fig. 7(a) presents the potentiodynamic polarization curves of 20SiMn steel immersed in S0 for 0.5 h and in S1 for different time. The corrosion parameters can be fitted by Tafel extrapolation of both the cathodic and anodic polarization curves. The corresponding electrochemical parameters such as the corrosion potential (E_{corr}), corrosion current density (I_{corr}), anodic Tafel slope (β_a), cathodic Tafel slope (β_c) and the inhibition efficiency (η%) are listed in Table 3. As can be seen, after introducing IP6 (S1), the current density (I_{corr}) firstly increases at 0.5 h and then significantly decreases. Correspondingly, the inhibition efficiency (η%) calculated by Eq. (4) is a negative value at 0.5 h and then gradually increases to more than 90% after immersion for 24 h.

In the case of immersed in S0 for 0.5 h, there is an active dissolution in the anodic branch and a Tafel behavior in the cathodic branch. Different from that in S0, the polarization curve in S1 for 0.5 h shows an active–passive behavior in anodic region and a limiting diffusion behavior in cathodic region. Furthermore, the anodic current density decreases while the cathodic current density increases comparing to that in S0. This can be explained as that the reduction of oxygen to OH^- is the domain cathodic reaction in the alkalescent buffer solution for steel rebar corrosion. According to the literature [51], IP6 exists in the form of phytate irons ($C_6H_6(H_6P_6O_{24})_6^-$ and $(C_6H_6(H_4P_6O_{24})_8^-$) by releasing 6 or 8 protons in neutral solution. In the active region, as soon as the steel electrode dissolves, phytate ions would chelate with the dissolved

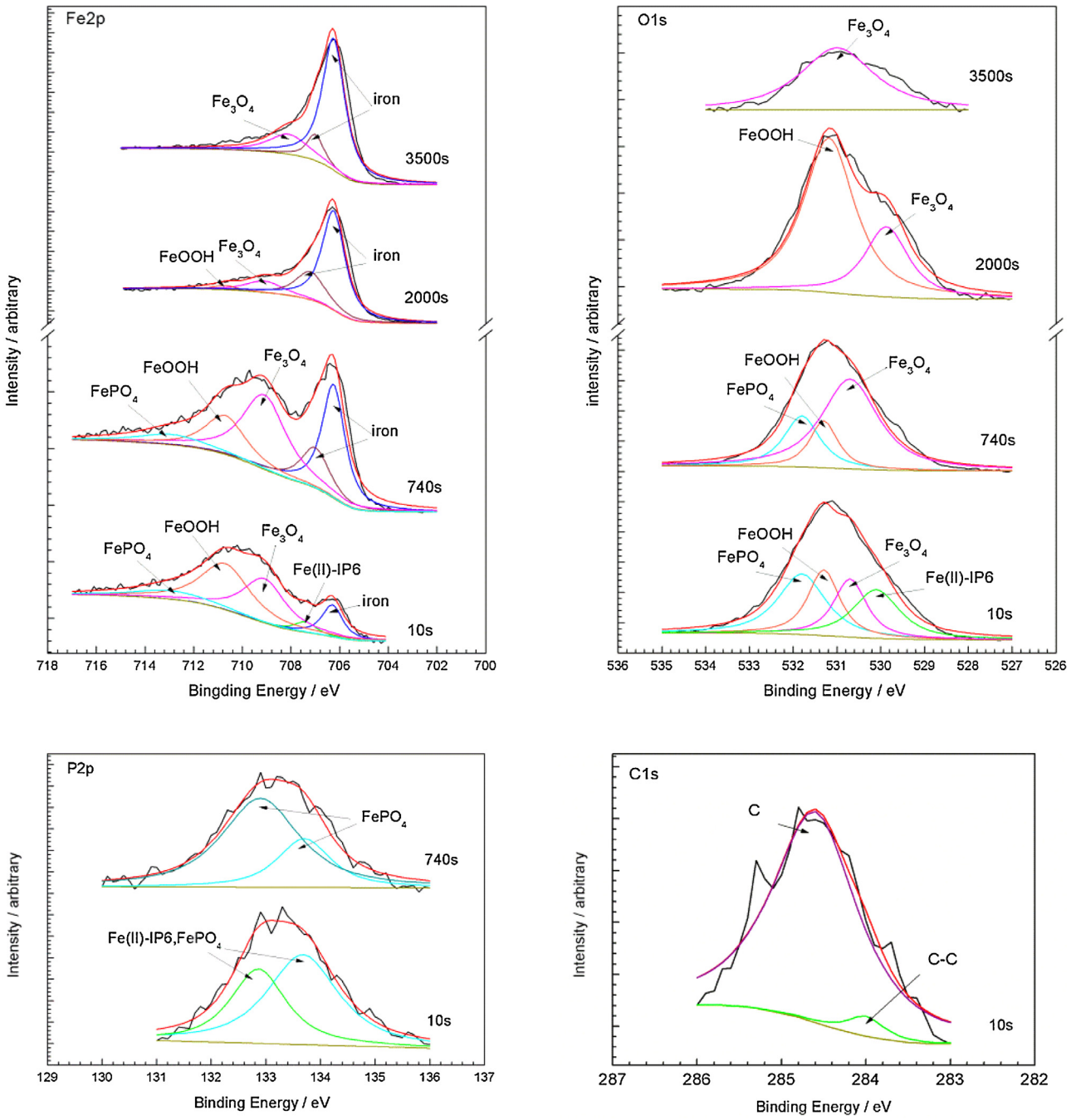

Fig. 6. XPS high-resolution spectra of Fe2p,O1s, P2p, C1s of the deposited film on specimen in the presence (S1) of 5.30 mmol/L IP6, recorded in (0.045 mol/L $NaHCO_3$ + 0.005 mol/L Na_2CO_3 + 0.6 mol/L NaCl) solution.

Table 3
Corrosion parameters obtained from potentiodynamic polarization curves for specimens in the absence (S0) and presence (S1) of 5.30 mmol/L IP6 for different immersion time, recorded in (0.045 mol/L $NaHCO_3$ + 0.005 mol/L Na_2CO_3 + 0.6 mol/L NaCl) solution.

Immersion time/h	E_{corr}/ mV/SCE	Icorr/ μA cm^{-2}	ν (mm/a)	β_c/mV dec^{-1}	β_a/mV dec^{-1}	η/%
S0, 0.5 h	−0.73	35.18	0.412	−343.7	111.5	–
S1, 0.5 h	−0.68	83.16	0.973	−267.5	275.6	−136.38
6 h	−0.58	13.94	0.163	−289.2	545.9	60.38
24 h	−0.71	0.19	0.002	−140.4	81.4	99.45
36 h	−90.70	0.52	0.006	−161.4	114.8	98.52
72 h	−0.61	0.34	0.004	-61.5	182.8	99.04

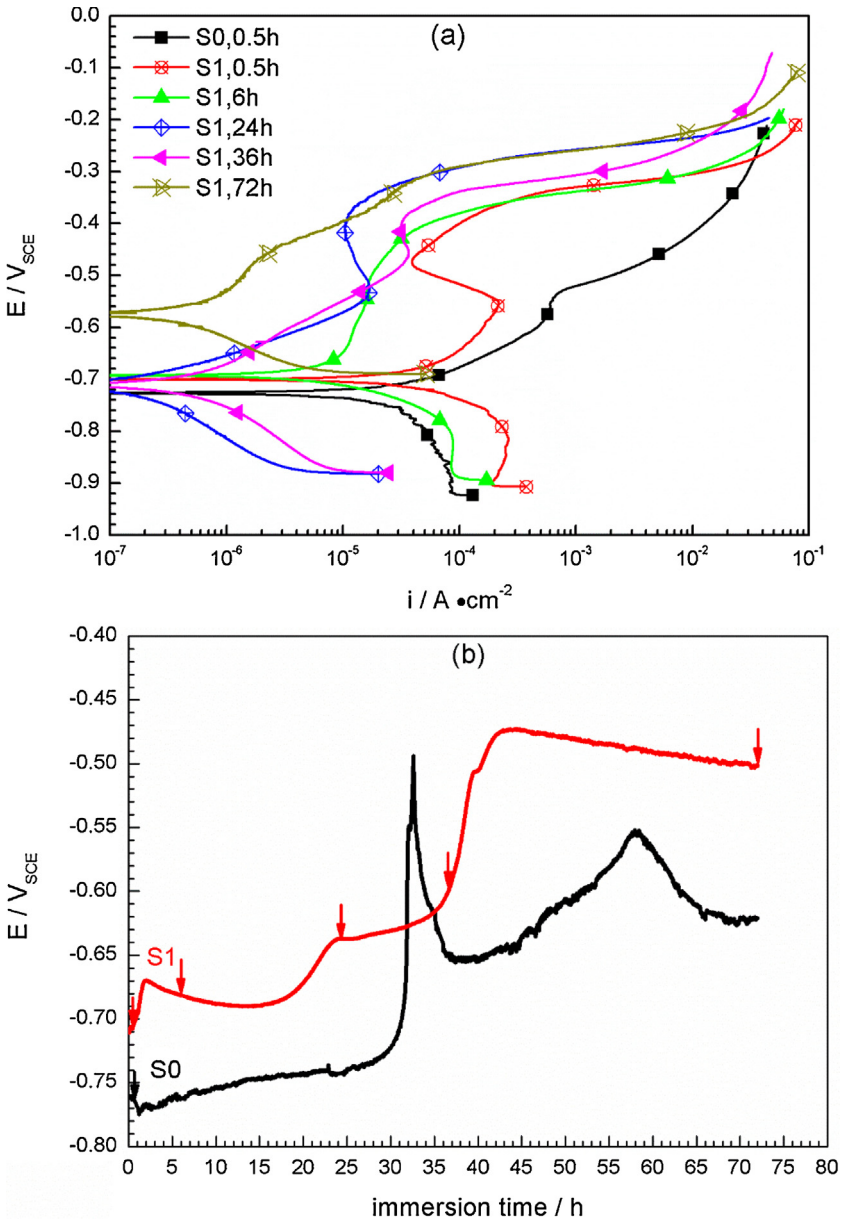

Fig. 7. Potentiodynamic polarization curves (a) and open circuit potentials (b) of specimens immersed in the absence (S0) and presence (S1) of 5.30 mmol/L IP6, recorded in (0.045 mol/L $NaHCO_3$ + 0.005 mol/L Na_2CO_3 + 0.6 mol/L NaCl) solution.

ferrous ions to form an insoluble precipitates Fe(II)-IP6 on the steel surface. The complex Fe(II)-IP6 could prevent the further dissolution of iron, causing the decrease of anodic current density. Besides, based on the analysis of XPS above, it is sure that IP6 has hydrolyzed. The general hydrolysis formula is described by [52]:

$$C_6H_6(OPO_3H_2)_6 + nH_2O \rightarrow C_6H_6(OH)_n(OPO_3H_2)_{(6-n)} + nH_3PO_4 \quad (8)$$

where n is the natural number ranging from 1 to 6. In S1 solution with pH8.89, HPO_4^{2-} is the main component in alkalescent buffer solution S1 [53]. Ferrous ion coming from anodic dissolution could be consumed by reacting with HPO_4^{2-} to form insoluble ferrous phosphate $FeHPO_4$:

$$Fe^{2+} + HPO_4^{2-} \rightarrow FeHPO_4 \quad (9)$$

As the potential increases to more positive, $FeHPO_4$ in the precipitated film is further oxidized to the Fe(III) compounds, $FePO_4$, leading to the passivation of the electrode:

$$FeHPO_4 \rightarrow FePO_4 + H^+ + e^- \quad (10)$$

In addition, ferrous ions are likely hydrolyzed to ferrous hydroxide, which can be oxidized to ferric oxide by air and precipitated as these oxides [16]:

$$6Fe(OH)_2 + O_2 \rightarrow 2Fe_3O_4 + 6H_2O \quad (11)$$

$$4Fe(OH)_2 + O_2 \rightarrow 4FeOOH + 2H_2O \quad (12)$$

Obviously, the accumulations of different precipitated species induce the inhibition effect on the anodic dissolution of the 20SiMn steel. However, the cathodic current density increases after the introduction of IP6 for 0.5 h, which may be ascribed to the electrochemical catalysis effect of Fe(II) compounds on the cathodic reduction.

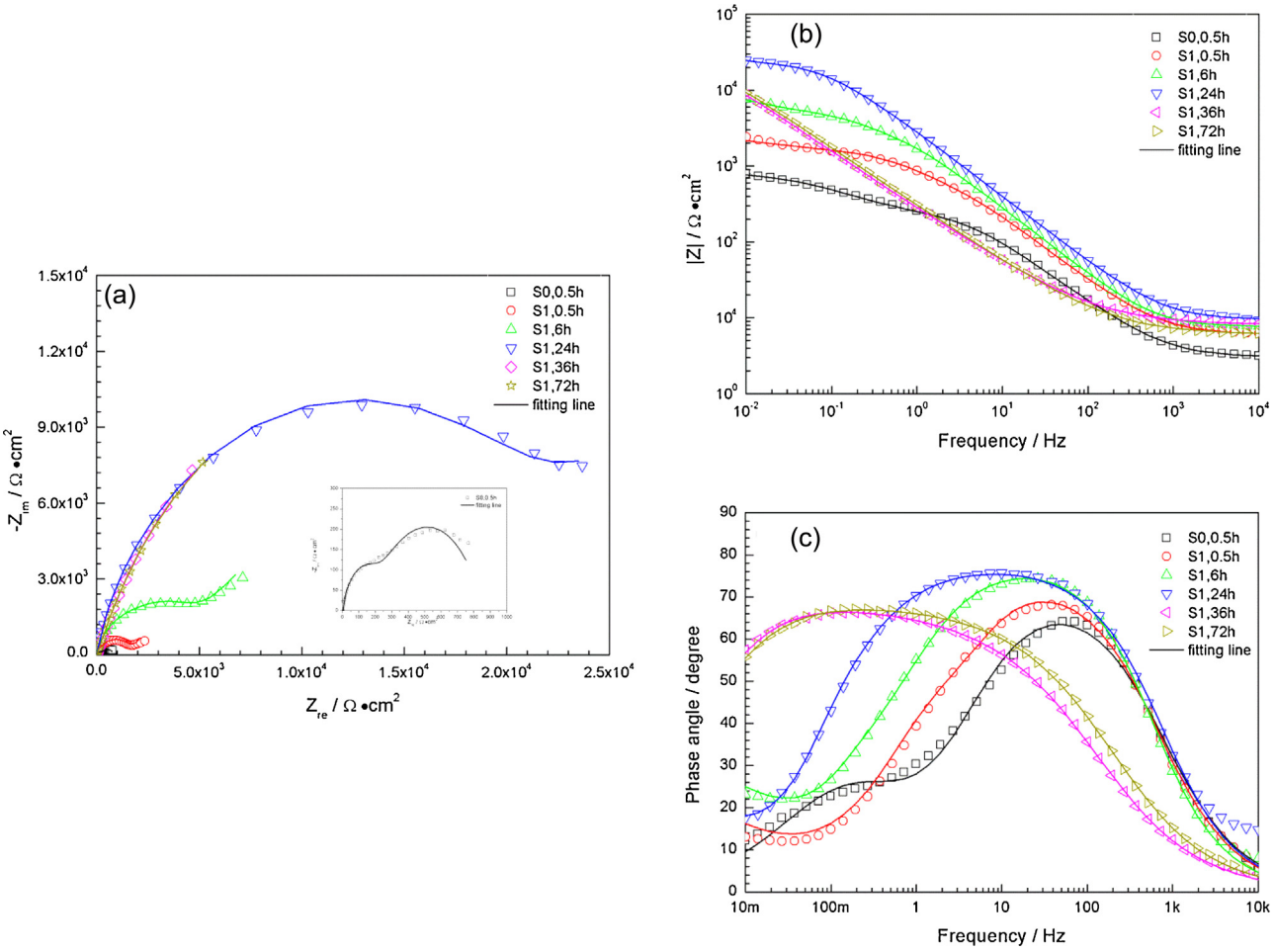

Fig. 8. EIS of specimens immersed in the absence (S0) and presence (S1) of 5.30 mmol/L IP6, recorded in (0.045 mol/L $NaHCO_3$ + 0.005 mol/L Na_2CO_3 + 0.6 mol/L NaCl) solution.

As the immersion time extends to 6 h in S1, the anodic behavior in polarization curve directly enters to the passive state without the active–passive transformation. This indicates that the anodized protective film has been formed at low polarized potential. On the other hand, the cathodic current density is still featured as a limiting diffusion process, showing a decreased current density comparing with that at 0.5 h. This is caused by the fact that the conversion of Fe(II)-IP6 to Fe(III) phosphates or oxides reduces the electrochemical catalysis activity of the steel surface. When the immersion time prolongs to 24 h, the current densities in both anodic and cathodic decrease significantly. The further decrease of the anodic current density should be ascribed to the enhanced blocking effect by the thickening and compacting of the deposited film, while the decrease in cathodic current should be caused by the disappearance of Fe(II)-IP6. Additionally, the anodic and cathodic branch respectively shows the Tafel relationship between the logarithmic current density and applied potential, suggesting that the cathodic process has already controlled by the charge transfer step of FeOOH reduction to Fe_3O_4 on steel surface.

With the immersion time further prolongs to 36 h, the anodic current density shows almost no change but the cathodic current density starts to increase comparing with that at 24 h. After immersion for 72 h, the anodic current density dramatically decreases while the cathodic current density continued to increase. The further weakening of the anodic current density should be caused by the formation of more Fe_3O_4 in the film, which makes the film more compact; the enhancement of the cathodic current density should be ascribed to the larger quantity of FeOOH formed in the film, which can accelerate the electrochemical reduction rate during the cathodic potential sweep. Specifically, FeOOH could be reduced to Fe_3O_4 by Eq. (13):

$$8FeOOH + Fe^{2+} + 2e^- \rightarrow 3Fe_3O_4 + 4H_2O \quad (13)$$

This is responsible for the slight enhancement of the corrosion current density and the sudden rise of OCP shown in Fig. 7b. Besides, during the whole immersion period, the OCP in S1 is higher than that in S0, and the breakdown potential *E*b in S1 is also higher than that in S0, implying that the pit corrosion resistance of the deposited film increases gradually.

3.4.2. *Electrochemical impedance spectroscopy (EIS)*

Fig. 8 presents the EIS results of the 20SiMn steel immersed in S0 and S1 solutions, respectively. The arrows as marked in Fig. 7b represent the time nodes of EIS measurement. Accordingly, the negligible OCP change describes that the cell system is satisfied to the requirement of steady state for the EIS measurement. It can be observed that after 0.5 h immersion, the Nyquist plot in S0 (the enlarged one inserted in Fig. 8a) shows two capacitive semicircles within the studied frequency range. However, the shape of EIS is changed by the introduction of IP6. According to the characteristics of EIS in S1, the evolution process could be divided into two stages: the early stage of 0–24 h and the later stage of 24–72 h. All of the Nyquist plots in the early stage show a depressed semicircle at high frequency region, followed by a diffusion tail at low frequency region (Warburg impedance). The presence of Warburg impedance indicates that the electrochemical reactions become diffusion-

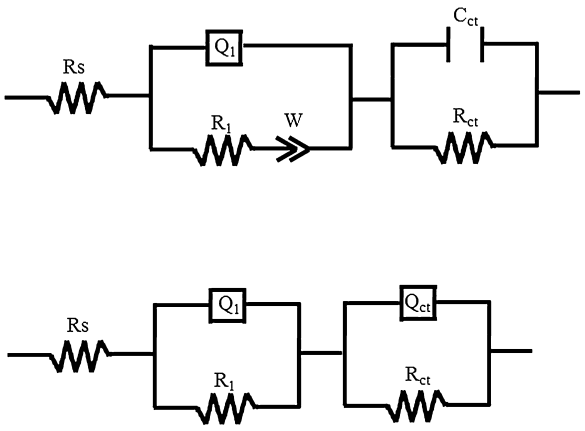

Fig. 9. Fitting circuits of EIS for specimens in the absence (S0) and presence (S1) of 5.30 mmol/L IP6, recorded in (0.045 mol/L $NaHCO_3$ + 0.005 mol/L Na_2CO_3 + 0.6 mol/L NaCl) solution.

controlled, which is in agreement with the polarization curve at 0.5 h (Fig. 7a). Additionally, with extending immersion time, the diameter of the semicircle at high frequency region enlarges while the diffusion tail at low frequency shortens. After 36 h immersion, the diffusion tail completely vanishes, and the evolution process enters the later stage. In this stage, the Nyquist plots characterizes as a segment of arc with a larger radius 23.

It could be seen from the Bode plots (Fig. 8c) that there are two time constants for all spectra in S1, as well as that in S0 for 0.5 h. Combining with the structure analysis of SEM and XPS above, the equivalent circuits R(Q(RW))(CR) and R((QR)(QR)) (Fig. 9) are chosen for a better fitting of the EIS data at early and later stage in S1, respectively. The spectrum in S0 for 0.5 h immersion is also fitted by the equivalent circuit R((QR)(QR)), where *Rs* is the solution resistance, *Q*1 the constant phase element (CPE) of the film, *R*1 the rust layer film in S0 and film resistance in S1, W the Warburg impedance, C_{ct} the capacitance of electric double layer, Q_{ct} the constant phase element (CPE) of the electric double layer, and R_{ct} the charge transfer resistance of the steel interface. With the forming of deposited film on the metal surface, the electric double layer is gradually deviating from the pure capacitance. Therefore, in the second stage in S1, Q_{ct} is chosen to replace C_{ct}. The impedance function of a CPE complies with the following equation:

$$Z_{CPE} = Y_0^{-1}(j\omega)^{-n} \quad (14)$$

where Y_0 is the CPE constant, ω the angular frequency (in rad/s), j the imaginary unit and n is a CPE exponent which can be used as a gauge of the heterogeneity or roughness of the surface [54].

Table 4 presents the fitting results. As can be seen, the presence of IP6 in S1improves the value of *R*1 greatly comparing with that in S0. With increasing of immersion time, both *R*1 and R_{ct} in S1 increases monotonically and reaches a magnitude of around $10^4\ \Omega\,cm^2$ at 24 h. This is related to the structure and composition of the deposited film on the surface of steel. Besides the increased thickness of this deposited film, the improved corrosion resistance of this film could also be ascribed to the larger quantities of Fe_3O_4, which is converted from FeOOH as described by Eq. (13). At the same time, this compact deposited film strongly suppresses the electrochemical reactions at the double layer, and is responsible for the increased *R*ct value. On the other hand, the Warburg impedance *W* decreases gradually, suggesting that the influence of diffusion process attenuated with the completing of the deposited film. Moreover, Table 4 also lists the corrosion rates and inhibition efficiencies calculated by Eqs. (6) and (7), respectively. Comparing with the corrosion rate in S0, 0.468 mm/a, the addition of IP6 does not suppress the corrosion of 20SiMn steel thoroughly, while even

Table 4
Fitting results of EIS of specimens immersed in the absence (S0) and presence (S1) of 5.30 mmol/L IP6 for different immersion time, recorded in (0.045 mol/L $NaHCO_3$ + 0.005 mol/L Na_2CO_3 + 0.6 mol/L NaCl) solution.

Immersion time/h	Rs/kΩ cm^2	Q1-Y_0 × 10^4/F cm^{-2}	n1	R1/kΩ cm^2	W × 10^4/Ω^{-1} cm^{-2} s$^{-0.5}$	C_{ct} × 10^4/F cm^{-2}	Q_{ct}-Y_0 × 10^4/F cm^{-2}	nct	R_{ct}/kΩ cm^2	I_{corr} μA cm^{-2}	ν(mm/a)	η/%
S0, 0.5 h	0.003	3.23	0.85	0.20	–	–	31.12	0.70	0.65	40.00	0.468	–
S1, 0.5 h	0.006	2.11	0.81	1.51	52.12	2.92	–	–	0.11	236.36	2.765	−490.91
6 h	0.008	0.99	0.88	2.80	9.58	7.20	–	–	1.36	19.12	0.224	52.21
24 h	0.009	1.00	0.83	9.67	5.42	1.87	–	–	10.77	2.41	0.028	93.96
36 h	0.008	14.04	0.84	22.61	–	–	23.64	0.62	13.17	1.97	0.023	95.06
72 h	0.006	10.63	0.81	25.77	–	–	32.86	0.61	15.77	1.65	0.019	95.88

promotes the corrosion in the initial stage. Correspondingly, the inhibition efficiency at 0.5 h is negative, which could be ascribed to the electrochemical catalysis effect of Fe(II)-IP6 as mentioned above. Afterwards, the corrosion rate gradually decreases to around 0.02 mm/a, and the inhibition efficiency increases to more than 90%, providing a significant inhibition effect on the steel corrosion. The efficiency of IP6 can probably be maintained stable during a longer immersion due to the compact structure of the deposited layer. The results of EIS confirms the effectiveness of IP6 as an inhibitor for steel rebar in carbonated simulated concrete solutions contaminated by Cl^-.

The trend of inhibition efficiencies (η) acquired by EIS is in agreement with that by potentiodynamic polarization curves (Tables 3 and 4). The small difference of η values between these two methods could be attributed to the inevitable errors of fitting processes. On the other hand, the value of η obtained from weight loss measurement is in the range of those from electrochemical methods. It is quite reasonable considering that η obtained from weight loss measurement is a mean value, while those from electrochemical methods are the instantaneous ones. They both demonstrate the effect of the inhibitor.

The current work has just focused on investigating the inhibition effect of IP6 in a simulated carbonated pore solution. In real concrete pore solutions, the released free Ca^{2+} from $CaCO_3$ may make two kinds of effects on the inhibition behavior of IP6. Firstly, it can influence the ionization equilibrium reaction between bicarbonate and carbonate ions due to the precipitate of $CaCO_3$, leading to the concentration change of bicarbonate and carbonate ions; secondly, it can probably consume part of IP6 due to the formation of the insoluble complex of calcium phytate, and/or the sediment of $CaHPO_4$ by reacting with HPO_4^{2-} hydrolyzed from IP6. However, this consumption can be compensated by increasing the concentration of IP6.

It is certainly that we need to concern the inhibition effect of inhibitor on the passive steel rebar in the saturated $Ca(OH)_2$ solution (pH 12.6) simulating the concrete pore solution without carbonation. It is believed that to maintain the passivity of the steel rebar with suitable inhibitor is also a promising technique for life extension of the reinforced concrete structures.

4. Conclusions

Effects of IP6 on the corrosion of 20SiMn steel in simulated concrete solution contaminated by Cl^- have been studied. Based on the obtained data and above analysis, following conclusions are drawn:

(1) IP6 makes an effective inhibitor on 20SiMn steel rebar in simulated concrete solutions by the formation of a chemical conversion film.
(2) The chemical conversion film is of a three layer structure. The inner layer is constituted of Fe_3O_4 and FeOOH, and the middle layer of Fe_3O_4, FeOOH, and $FePO_4$, and the outer layer of Fe_3O_4, FeOOH, $FePO_4$, and Fe(II)-IP6.
(3) The inhibition process of IP6 can be divided into two stages. The first stage corresponds to a limiting diffusion-controlled process, and another stage is controlled by the charge transfer step.

Acknowledgment

This work was supported by the National Natural Science Foundation of China (No. 51471175).

References

[1] P. Ghods, O. Burkan Isgor, F. Bensebaa, D. Kingston, Angle-resolved XPS study of carbon steel passivity and chloride-induced depassivation in simulated concrete pore solution, Corros. Sci. 58 (2012) 159–167.
[2] S. Jones, N. Martys, Y. Lu, D. Bentz, Simulation studies of methods to delay corrosion and increase service life for cracked concrete exposed to chlorides, Cem. Concr. Comp. 58 (2015) 59–69.
[3] B. Huet, V. L'Hostis, F. Miserque, H. Idrissi, Electrochemical behavior of mild steel in concrete: influence of pH and carbonate content of concrete pore solution, Electrochim. Acta 51 (2005) 172–180.
[4] Y.T. Tan, S.L. Wijesinghe, D.J. Blackwood, The inhibitive effect of bicarbonate and carbonate ions on carbon steel in simulated concrete pore solution, Corros. Sci. 88 (2014) 152–160.
[5] M. Moreno, W. Morris, M.G. Alvarez, G.S. Duffó, Corrosion of reinforcing steel in simulated concrete pore solutions: effect of carbonation and chloride content, Corros. Sci. 46 (2004) 2681–2699.
[6] S.B. Farina, G.S. Duffo, Corrosion of zinc in simulated carbonated concrete pore solutions, Electrochim. Acta 52 (2007) 5131–5139.
[7] J.M. Gaidis, A.M. Rosenberg, The inhibition of chloride-induced corrosion reinforced-concrete by calcium nitrite, Abstr. Pap. Am. Chem. Soc. 187 (1984), 131-INDE.
[8] K.K. Sideris, A.E. Savva, Durability of mixtures containing calcium nitrite based corrosion inhibitor, Cem. Concr. Comp. 27 (2005) 277–287.
[9] M.C. Li, M. Royer, D. Stien, A. Lecante, C. Roos, Inhibitive effect of sodium eperuate on zinc corrosion in alkaline solutions, Corros. Sci. 50 (2008) 1975–1981.
[10] A. La Iglesia, V.M. La Iglesia, S. Fajardo, P.P. Gómez, J.M. Bastidas, Reaction between sodium monofluorophosphate and portlandite and impact on steel reinforcement corrosion inhibition, Constr. Build. Mater. 37 (2012) 46–50.
[11] H.E. Jamil, M.F. Montemor, R. Boulif, A. Shriri, M.G.S. Ferreira, An electrochemical and analytical approach to the inhibition mechanism of an amino-alcohol-based corrosion inhibitor for reinforced concrete, Electrochim. Acta 48 (2003) 3509–3518.
[12] M. Ormellese, L. Lazzari, S. Goidanich, G. Fumagalli, A. Brenna, A study of organic substances as inhibitors for chloride-induced corrosion in concrete, Corros. Sci. 51 (12) (2009) 2959–2968.
[13] S.M. Abd El Haleem, S. Abd El Wanees, A. Bahgat, Environmental factors affecting the corrosion behaviour of reinforcing steel. VI. Benzotriazole and its derivatives as corrosion inhibitors of steel, Corros. Sci. 87 (2014) 321–333.
[14] S.M. Abd El Haleem, S. Abd El Wanees, E.E. Abd El Aal, A. Diab, $Ca(OH)_2$,HPO42-Environmental factors affecting the corrosion behavior of reinforcing steel. IV. Variation in the pitting corrosion current in relation to the concentration of the aggressive and the inhibitive anions, Corros. Sci. 52 (2010) 1675–1683.
[15] C.L. Page, Aspects of the performance of corrosion inhibitors applied to reinforced concrete, in: Proceedings of the Ninth European Symposium on Corrosion Inhibitors, Italy: University of Ferrara, 2000.
[16] J.M. Gaidis, Chemistry of corrosion inhibitors, Cem. Concr. Com. (26 2004) 181–189.
[17] F. Wombacher, U. Maeder, B. Marazzani, Aminoalcohol based mixed corrosion inhibitors, Cem. Concr. Com. 26 (2004) 209–216.
[18] X. Zhou, H. Yang, F. Wang, Investigation on the inhibition behavior of a pentaerythritol glycoside for carbon steel in 3.5% NaCl saturated $Ca(OH)_2$ solution, Corros. Sci. 54 (2012) 93–200.
[19] J. Su, X.L. Wu, C.P. Yang, J.S. Lee, J. Kim, Y.G. Guo, Self-assembled LiFePO4/C Nano/Microspheres by using phytic acid as phosphorus source, J. Phys. Chem. C 116 (2012) 5019–5024.
[20] Y.-H. Wang, J.-B. He, Corrosion inhibition of copper by sodium phytate in NaOH solution: cyclic voltabsorptometry for in situ monitoring of soluble corrosion products, Electrochim. Acta 66 (2012) 45–51.
[21] J.-B. He Y. Li, M. Zhang, Corrosion inhibition effect of sodium phytate on brass in NaOH media. Potential-resolved formation of soluble corrosion products, Corros. Sci. 74 (2013) 116–122.
[22] Y.-H. Wang, J.-B. He, Corrosion inhibition of copper by sodium phytate in NaOH solution: Cyclic voltabsorptometry for in situ monitoring of soluble corrosion products, Electrochim. Acta 66 (2012) 45–51.
[23] C. Hao, R.-H. Yin, Z.-Y. Wan, Q.-J. Xu, G.-D. Zhou, Electrochemical and photoelectrochemical study of the self-assembled monolayer phytic acid on cupronickel B30, Corros. Sci. 50 (2008) 3527–3533.
[24] C. -c, X.- Li, S. Guo, P. Shen, T. Song, Y. Xu, H.-F.Y. Wen, Adsorption and corrosion inhibition of phytic acid calcium on the copper surface in 3 wt% NaCl solution, Corros. Sci. 83 (2014) 147–154.
[25] S. Shen, J. Du, X. -y, Y. Guo, H.-F.Y. Wen, Adsorption behavior of pH-dependent phytic acid micelles at the copper surface observed by Raman and electrochemistry, Appl. Surf. Sci. 327 (2015) 116–121.
[26] Y. X. Cui, Q. Li, G. Li, M. Jin, F. Wang Ding, Influence of phytic acid concentration on performance of phytic acid conversion coatings on the AZ91D magnesium alloy, Mater. Chem. Phys. 111 (2008) 503–507.
[27] X. F. Pan, D. Zhang Yang, Chemical nature of phytic acid conversion coating on AZ61 magnesium alloy, Appl. Surf. Sci. 255 (2009) 8363–8371.
[28] X. Guo, K. Du, Q. Guo, Y. Wang, R. Wang, F. Wang, Effect of phytic acid on the corrosion inhibition of composite film coated on Mg–Gd–Y alloy, Corros. Sci. 76 (2013) 129–141.
[29] E.-H. Han H. Shi, F. Liu, Protection of 2024-T3 aluminium alloy by corrosion resistant phytic acid conversion coating, Appl. Surf. Sci. 280 (2013) 325–331.
[30] Y. H. Yang, Y. Yang, H. Yang, Z. Liu, G. Zhang, R. Yu Shen, Formation of inositol hexaphosphate monolayers at the copper surface from a Na-salt of phytic acid solution studied by in situ surface enhanced Raman scattering spectroscopy,

Raman mapping and polarization measurement, Anal. Chim. Acta 548 (2005) 159–165.
[31] S. Shen, X. -y, P. Guo, Y.-C.P. Song, H.- an, Y. Wang, H.-F.Y. Wen, Phytic acid adsorption on the copper surface: observation of electrochemistry and Raman spectroscopy, Appl. Surf. Sci. 276 (2013) 167–173.
[32] M.A. Chidiebere, E.E. Oguzie, L. Liu, Y. Li, F. Wang, Corrosion inhibition of Q235 mild steel in 0.5 M $H2SO_4$ solution by phytic acid and synergistic iodide additives, Ind. Eng. Chem. Res. 53 (2014) 7670–7679.
[33] A.-R. El-Sayed, U. Harm, K.-M. Mangold, W. Fürbeth, Protection of galvanized steel from corrosion in NaCl solution by coverage with phytic acid SAM modified with some cations and thiols, Corros. Sci. 55 (2012) 339–350.
[34] S. X. Zheng, W. Zhang, M. Li, L. Yin Gong, Experimental and theoretical studies of two imidazolium-based ionic liquids as inhibitors for mild steel in sulfuric acid solution, Corros. Sci. 95 (2015) 168–179.
[35] M.K. Nieuwoudt, J.D. Comins, I. Cukrowski, The growth of the passive film on iron in 0. 05 M NaOH studied in situ by Raman micro-spectroscopy and electrochemical polarisation. Part I: near-resonance enhancement of the Raman spectra of iron oxide and oxyhydroxide compounds, J. Raman Spectrosc. 42 (2011) 1335–1339.
[36] R.L. Frost, M.L. Weier, K.L. Erickson, O. Carmody, S.J. Mills, Raman spectroscopy of phosphates of the variscite mineral group, J. Raman Spectrosc. 35 (2004) 1047–1055.
[37] J. Feng, X.J. Sun, J. Zhu, W. Xia, H. Liu, H.F. Yang, Surface enhanced Raman scattering spectra of phytic acid in the sol silver oxide, Spectrosc. Spect Anal. 26 (2006) 858–860.
[38] D.D. Hawn, B.M. DeKoven, Deconvolution as a correction for photoelectron inelastic energy losses in the core level XPS spectra of iron oxides, Surf. Interface Anal. 10 (1987) 63–74.
[39] U. Rodriguesfilho, S. Vazjr, M. Felicissimo, M. Scarpellini, D. Cardoso, R. Vinhas, R. Landers, J. Schneider, B. McGarvey, M. Andersen, Heterometallic manganese/zinc-phytate complex as a model compound for metal storage in wheat grains, J. Inorg. Biochem. 99 (2005) 1973–1982.
[40] L. Freire, X.R. Nóvoa, M.F. Montemor, M.J. Carmezim, Study of passive films formed on mild steel in alkaline media by the application of anodic potentials, Mater. Chem. Phys. 114 (2009) 962–972.
[41] P. Marcus, J. Grimal, The anodic dissolution and passivation of NiCrFe alloys studied by ESCA, Corros. Sci. 33 (1992) 805–814.
[42] K. Kishi, J. Nishioka, Interaction of Fe/Cu (100), Fe-Ni/Cu (100) and Ni/Fe/Cu (100) surfaces with O2 studied by XPS, Surf. Sci. 227 (1990) 97–106.
[43] J.R. Lince, S.V. Didziulis, D.K. Shuh, T.D. Durbin, J.A. Yarmoff, Interaction of O_2 with the Fe0.84Cr 0. 16 (0 0 1) surface studied by photoelectron spectroscopy, Surf. Sci. 277 (1992) 43–63.
[44] Y. Barbaux, M. Dekiouk, D. Le Maguer, L. Gengembre, D. Huchette, J. Grimblot, Bulk and surface analysis of a Fe–PO oxydehydrogenation catalyst, App. Catal. A-Gen. 90 (1992) 51–60.
[45] T. Hanawa, M. Ota, Calcium phosphate naturally formed on titanium in electrolyte solution, Biomaterials 12 (1991) 767–774.
[46] X. Cui, Q. Li, Y. Li, F. Wang, G. Jin, M. Ding, Microstructure and corrosion resistance of phytic acid conversion coatings for magnesium alloy, Appl. Surf. Sci. 255 (2008) 2098–2103.
[47] H. Konno, Y. Yamamoto, Ylide-metal complexes. XIII. An X-ray photoelectron spectroscopic study of bis(dimethylsulfoxonium methylide) gold chloride, B. Chem. Soc. Jpn. 60 (1987) 2561–2564.
[48] L. Yohai, M. Vázquez, M.B. Valcarce, Phosphate ions as corrosion inhibitors for reinforcement steel in chloride-rich environments, Electrochim. Acta 102 (2013) 88–96.
[49] M. Reffass, R. Sabot, M. Jeannin, C. Berziou, P. Refait, Effects of phosphate species on localised corrosion of steel in $NaHCO_3$+NaCl electrolytes, Electrochim. Acta 54 (2009) 4389–4396.
[50] V. Sieber, H. Hildebrand, S. Virtanen, P. Schmuki, Investigations on the passivity of iron in borate and phosphate buffers, pH 8. 4, Corros. Sci. 48 (2006) 3472–3488.
[51] X. Gao, C. Zhao, H. Lu, F. Gao, H. Ma, Influence of phytic acid on the corrosion behavior of iron under acidic and neutral conditions, Electrochim. Acta 150 (2014) 188–196.
[52] J. Ma, J. Hong, M. Wu, Preparation of inositol by hydrolysis of phytic acid with microwave radiating in short time, J. Chin. Cereals Oils Assoc. 18 (2003) 78–84.
[53] R.E. Stauffer, D.E. Armstrong, Cycling of iron, manganese, silica, phosphorus, calcium and potassium in two stratified basins of Shagawa Lake, Minnesota, Geochim. Cosmochim. Acta 50 (1986) 215–229.
[54] A. Singh, I. Ahamad, V.K. Singh, M.A. Quraishi, Inhibition effect of environmentally benign Karanj (Pongamia pinnata) seed extract on corrosion of mild steel in hydrochloric acid solution, J. Solid State Electr. 15 (2011) 1087–1097.